Supplementary Information

Oxidation of Dibenzyl Ether with Nitric Acid to Benzaldehyde in Continuous-flow Microreactors

Xiang Li[a] Saier Liu[a] Minjing Shang[a*], Yuanhai Su[ab*]

[a]State Key Laboratory of Polyolefins and Catalysis, School of Chemistry and Chemical Engineering, Shanghai Jiao Tong University, Shanghai 200240, P. R. China.

[b]Key Laboratory of Thin Film and Microfabrication (Ministry of Education), Shanghai Jiao Tong University, Shanghai 200240, PR China

*Corresponding author. Tel.: +86 21-54738710, E-mail address: mshang@sjtu.edu.cn; y.su@sjtu.edu.cn.

S1. Product analysis methods

The tested samples mainly contain the reactant dibenzyl ether, the main product benzaldehyde, the by-product benzyl alcohol, the by-product benzoic acid, and the internal standard n-decane. The boiling points of all the products are below 325 ℃. Therefore, a high-performance gas chromatograph (Agilent 7890B, HP-5 column, 30 m×0.32 mm×0.25 μm) was adopted to analyze the products. The samples were quantitatively detected in combination with the internal standard method.

The operation method of the high-efficiency gas chromatograph in this project is as follows: Start the injection when the column temperature rises to 50 ℃, stay at 50 ℃ for 5 minutes, then increase the temperature at a rate of 10 ℃/min to 100 ℃, then increase the temperature at a rate of 25 ℃/min to 225 ℃, and finally increase the temperature at a rate of 50 ℃/min to 325 ℃ to end the detection.

According to the requirements of the experimental detection, a series of standard sample solutions were prepared. After gas chromatography analysis, a standard curve was plotted showing the ratio of the peak area of the internal standard substance to the ratio of the substance quantity of the internal standard. The molar ratios of each component of the standard sample to the internal standard are shown in Table S1. The standard curves of the molar ratios of each component to the internal standard relative to the peak area ratios of each component to the internal standard are shown in Figure S1. The gas chromatogram of standard sample 4 is shown in Figure S2.

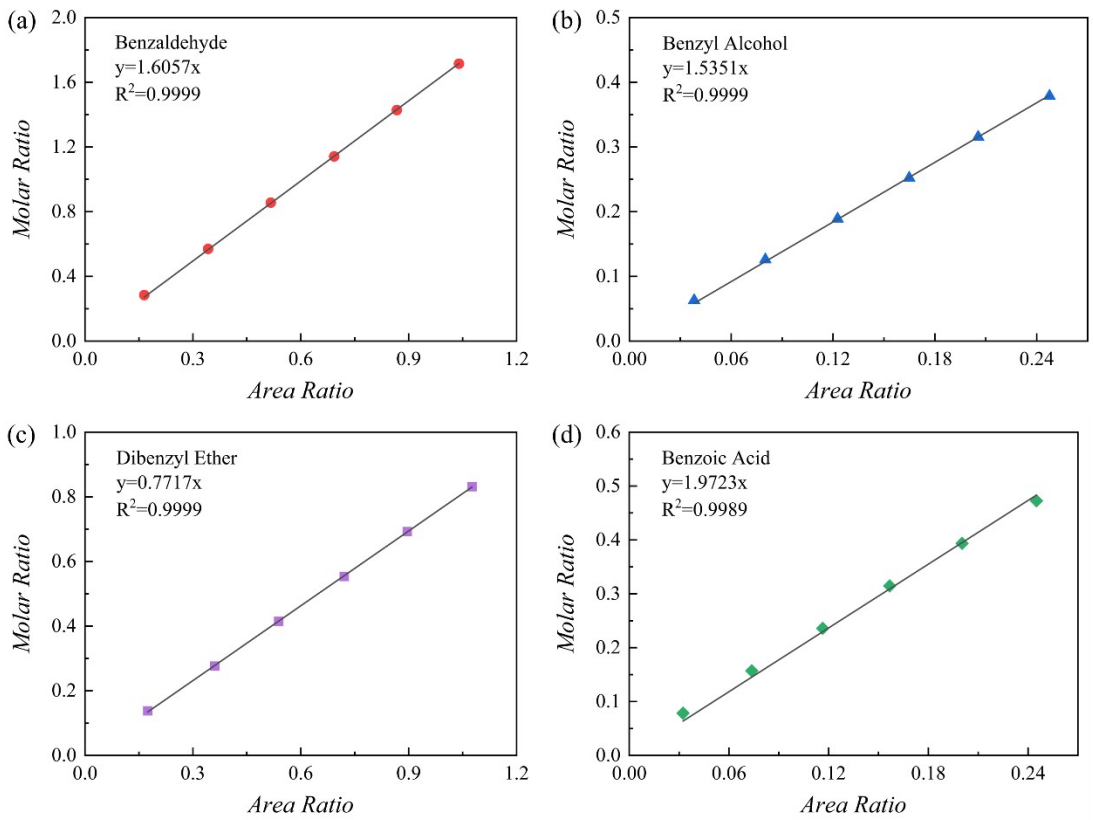

Figure S1 Standard curve of molar ratio of each component to internal standard with respect to peak area ratio of each component to internal standard. (a) Benzaldehyde; (b) Benzyl alcohol; (c) Dibenzyl ether; (d) Benzoic acid.

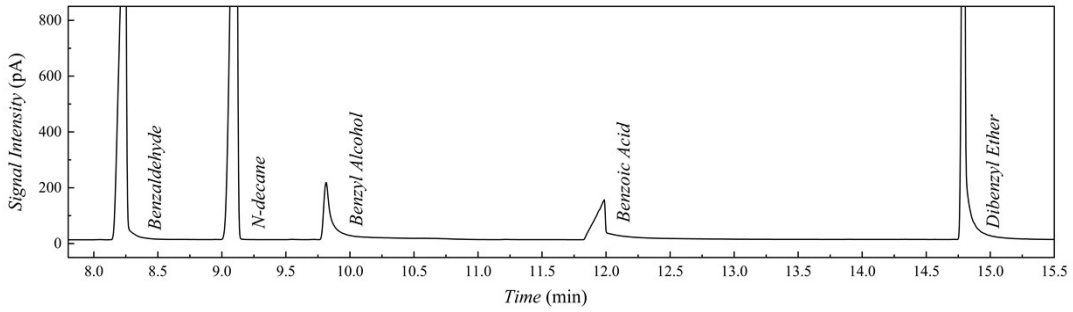

Figure S2 Sample 4 gas chromatogram.

Table S1 The molar ratio of each component of the standard sample to that of the internal standard

Sample Number	Benzaldehyde	Benzyl Alcohol	Benzoic Acid	Dibenzyl Ether
1	0.284871804	0.06291272	0.078510094	0.138124058
2	0.570114588	0.125907369	0.157122429	0.276427991
3	0.855729078	0.188984108	0.235837206	0.414912151
4	1.141716	0.252143096	0.314654624	0.55357689
5	1.428076085	0.315384497	0.393574885	0.692422561
6	1.714810061	0.378708469	0.47259819	0.83144952

S2. Analysis and exploration of flow patterns in capillary microreactors

To address the issue of low DBE conversion and low BzH yield in capillary microreactors, two strategies were attempted. One was to increase the molar ratio of the oxidant to the reactant by adjusting the flow rates of the aqueous and organic phases. The other was to increase the reaction residence time by extending the length of the capillary.

Liquid-liquid two-phase flow patterns in the capillary microreactor at different flow rates were observed using a microscopic high-speed camera system at room temperature, as shown in Figure S3. It can be seen that the aqueous and organic phases maintained a relatively stable liquid-liquid two-phase flow pattern. This is because the reaction hardly proceeded at room temperature and the immiscible liquid-liquid two phases formed segmented flow (namely slug flow) in the capillary microreactor.

From the flow patterns shown in Figure S3(a)-(c), it can be observed that the decrease of the flow rate of the organic phase with keeping the flow rate of the aqueous phase constant could result in a reduction in the length of the organic phase slugs and a significant increase in the length of the aqueous phase slugs, and the interfacial area gradually rose from 3.54×10^3 m^2/m^3 to 4.23×10^3 m^2/m^3. Figure S3(c)-(e) shows that the increase of the flow rate of aqueous phase with keeping the flow rate of the organic phase constant could lead to a substantial increase in the length of the aqueous phase slugs and a relatively constant length of the organic phase slugs, and the interfacial area gradually decreased from 4.23×10^3 m^2/m^3 to 4.13×10^3 m^2/m^3. This phenomenon

occurred because the aqueous phase acted as the dispersed phase and the organic phase served as the continuous phase. The length of the aqueous phase slugs always gradually expanded with decreasing the flow rate of the organic phase or increasing the flow rate of the aqueous phase, which was consistent with the literature.[1,2] For the slug flow, the interfacial area plays an important role in the mass transfer of liquid-liquid two-phase reaction systems. But the increased length of the aqueous phase slugs led to the decrease in the ratio of the interfacial area of two phases. Consequently, it is not possible to increase the molar ratio of the oxidant to the reactant by adjusting the flow rates of the aqueous and organic phases to enhance the reaction efficiency.

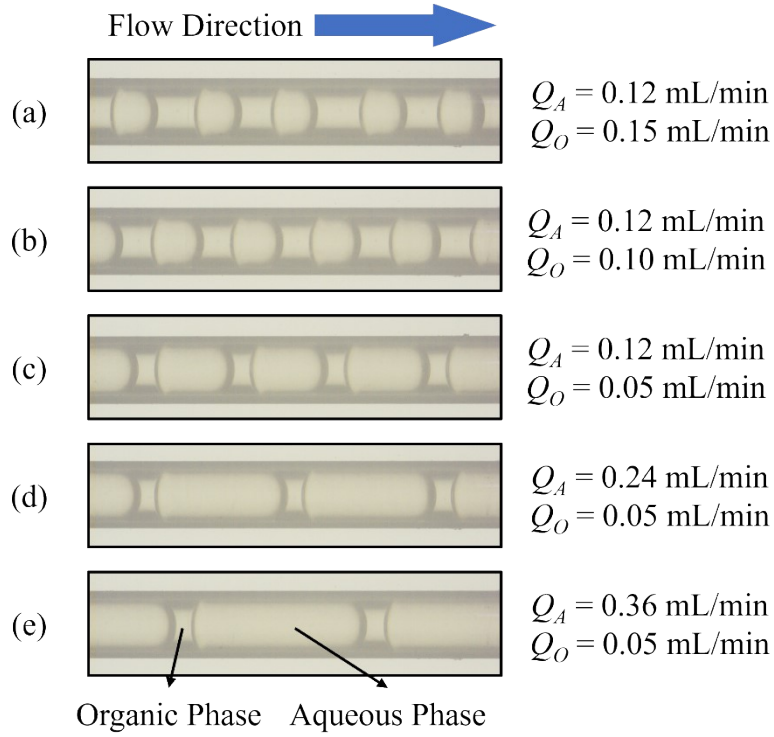

Figure S3 Photos of flow patterns at different flow rates in a capillary microreactor: T = 20 ℃, C_{HNO3} = 8 mol/L, C_{NaNO2} = 1 mol/L.

The liquid-liquid two-phase flow patterns in the capillary microreactor were also observed at 70 ℃ as shown in Figure S4 and Figure S5. The DBE and HNO3 solutions

initially formed a stable liquid-liquid two-phase slug flow pattern in the early stage of the reaction. There was an organic phase liquid film between the aqueous phase liquid segment and the inner wall of the capillary, so the organic phase was the continuous phase and the aqueous phase was the dispersed phase (Figure S5(a)). Nitrogen-containing gas as the product appeared and grew on the inner wall surface, forming a long bubble at the 3 m tubing length in Figure S4(a). Figure S5(d) is a schematic diagram of the flow pattern at this time. There was no organic phase liquid film between the bubble and the wall. Under the effect of the oleophilic wall, the tail of the downstream bubble separated from the organic phase. The organic phase liquid segment needed to "supplement" the liquid film when flowing through this area, so the organic phase was "retained" by the wall and had a relatively low average axial movement speed. Taking the overall liquid-liquid two-phase between adjacent bubbles as the reference system, the aqueous phase liquid segment had a relative velocity towards the downstream, eventually causing the aqueous phase to accumulate at the tail of the downstream bubble, while the organic phase cannot pass through the upstream bubble via the liquid film and accumulated at the head of the bubble, forming the long liquid segmented slug flow pattern shown in Figure S5(e). The change in the flow pattern leads to a significant decrease in the contact area between the liquid-liquid two phases.

The computational procedures for the specific interfacial area in the capillary microreactor under different experimental conditions are shown in Equations (1) and (2).

$$SIA = \frac{S}{V} = \frac{2\pi r^2 + L_A \times 2\pi r}{L \times \pi r^2} = \frac{2 \times (r + L_A)}{L \times r} \text{ * MERGEFORMAT (1)}$$

$$SIA = \frac{S}{V} = \frac{x\pi r^2}{L \times \pi r^2} = \frac{x}{L} \text{ * MERGEFORMAT (2)}$$

where r represents the radius of the capillary microreactor, L represents the total length of the repeated liquid phase unit, L_A represents the length of the aqueous phase liquid segment, and x represents the number of interfaces where the oil and aqueous phases come into contact.

In the initial stage without gas production, L_A was 1.81 mm, L was 2.61 mm, and the calculated specific interfacial area was 3.54×10^3 m^2/m^3 (Equation (1)). At the 3 m tubing length in Figure S4(a), the length between two bubbles was 13.03 mm, and the specific interfacial area was 0.23×10^3 m^2/m^3 (Equation (2)), which was only 6.5% of the initial stage. In addition, the appearance and growth of gas bubbles were uncontrolled, and sometimes there was only the organic phase (or aqueous phase) between adjacent bubbles, with the bubbles completely separating them from the aqueous phase (or organic phase). Therefore, when conducting such multi-phase reactions accompanied by gas generation in a capillary microreactor, the adverse effects of the generated gas on the reaction are twofold: the gas occupies a large amount of space in the reactor, reducing the effective reaction volume and the residence time of the reaction liquid being significantly less than the space time; the generated gas has a significant impact on the contact form of the liquid-liquid two phases, causing the originally stable slug flow with high specific interfacial area to change, and the mass

transfer area to decrease significantly.

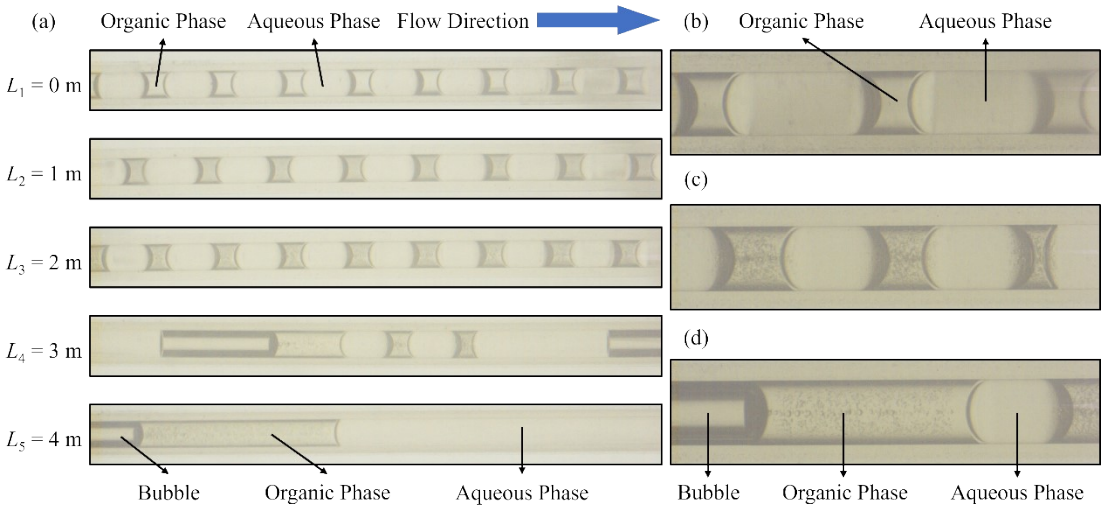

Figure S4 Photos of the variation of the flow patterns along the capillary microreactor: (a) Whole photograph; (b) Local photograph of L_1; (c) Local photograph of anterior of L_4; (d) Local photograph of posterior of L_4.

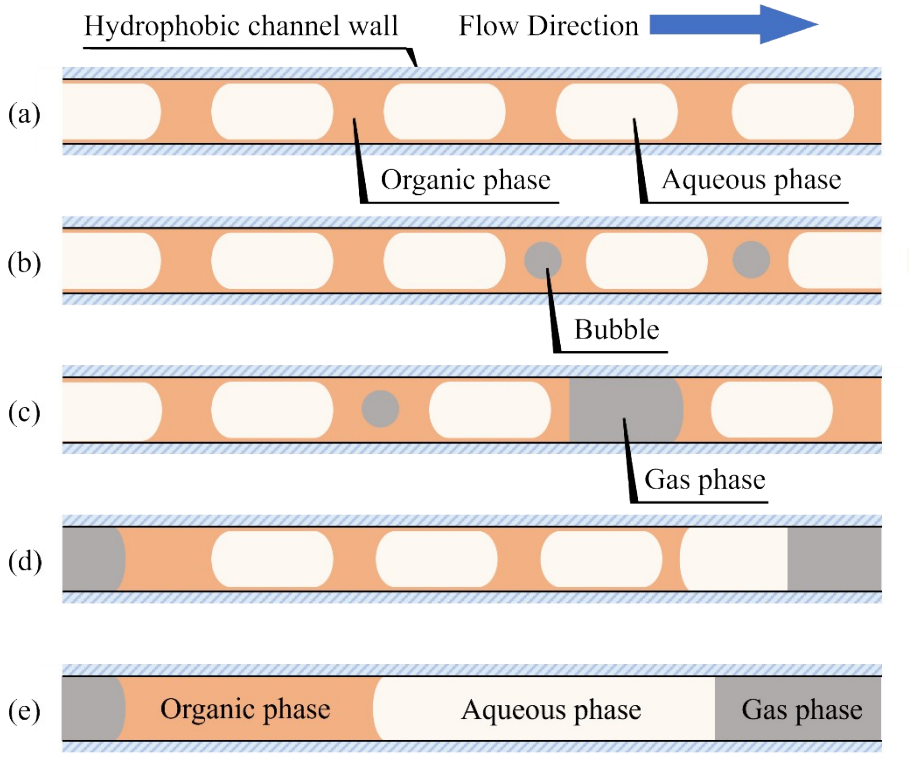

Figure S5 Schematic diagram of the variation of the flow patterns along the capillary microreactor: (a) Initial stage of the reaction; (b) Bubble formation stage; (c) Gas phase generation stage; (d) Two phases moving stage; (e) Final stage of the reaction.

S3. Post-treatment methods for samples

In advance, about 0.9g (weighed and recorded) of n-decane was added to the beaker containing the sample as the internal standard solution. Then, about 10 mL of 21.57% sodium chloride solution was added. On the one hand, it was used to dilute the unreacted nitric acid and quench the reaction. On the other hand, the water-soluble substances in the organic products were washed out by water.

After receiving the sample, 70 mL of n-hexane solution was added to dilute the sample and the internal standard. The aqueous phase and the organic phase were separated using a separating funnel. Then, 5 mL of a 21.57% sodium chloride solution was added to the separating funnel twice to wash the product with water. After sampling, the sample was sent to the high-performance gas chromatograph for analysis.

S4. The space-time yield of three different reactors

According to the calculation, the space-time yield of the packed-bed microreactor was approximately twice that of the capillary microreactor and 40 times that of the batch reactor. The calculation method is shown in Equation (3).

$$STY = \frac{n_{BzH}}{t \times V} \quad \text{* MERGEFORMAT (3)}$$

where n_{BzH} represents the molar number of BzH, t represents the reaction time, V represents the reactor volume. The specific data are shown in Table S2.

Table S2 The space-time yield of three different reactors

Reactor	t (h)	V (L)	n_{BzH} (mol)	STY (mol·L^{-1}·h^{-1})
Batch reactor	2	0.5	0.148	0.148
Capillary microreactor	0.1	8.242×10^{-3}	3.936×10^{-3}	2.865
Packed-bed microreactor	0.1	8.494×10^{-3}	7.939×10^{-3}	5.608

S5. Particle size distribution of the glass beads

Three different sizes of glass beads, namely 104.5 μm, 167.9 μm and 380.2 μm in average, were applied to fill the packed-bed microreactor. The physical diagrams of the glass beads and the data on their particle size distribution are shown in the Figure S6.

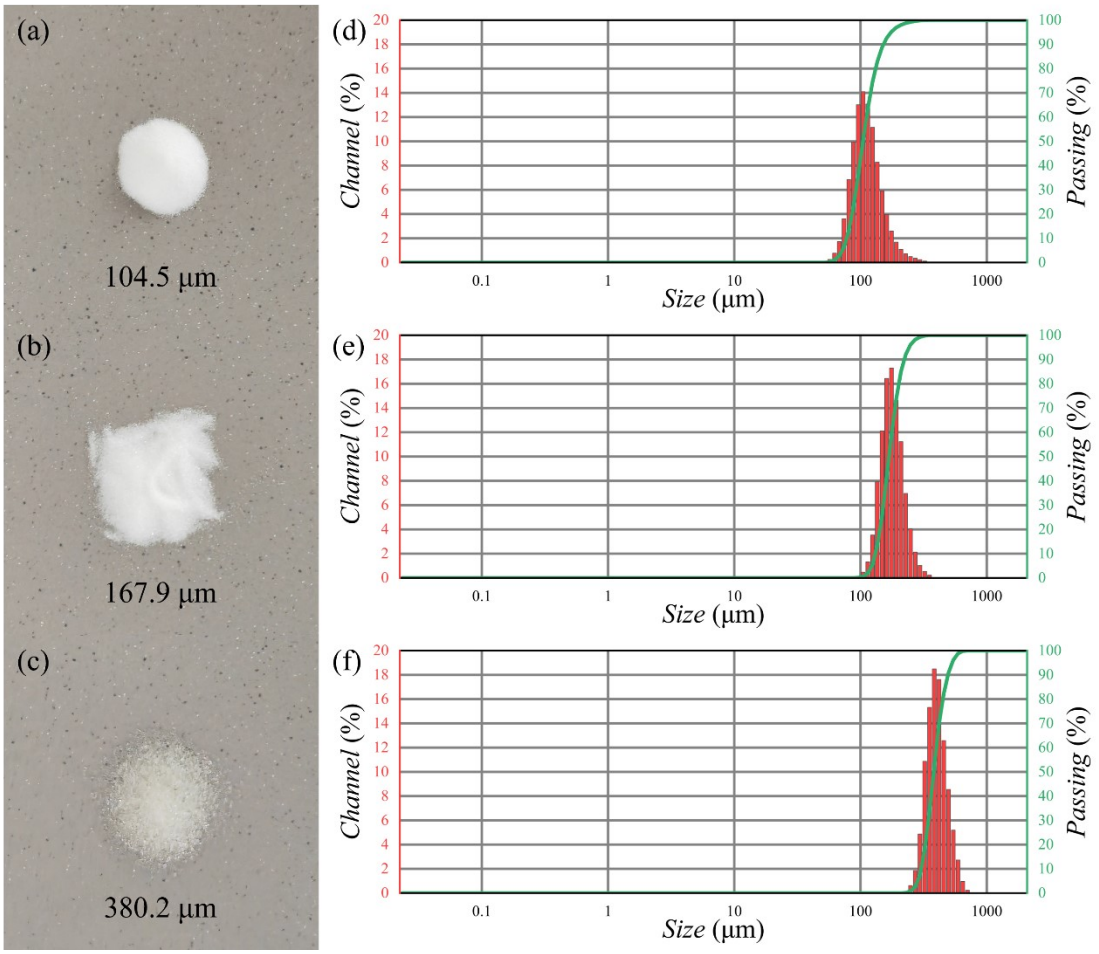

Figure S6 The physical diagrams of the glass beads: (a) 104.5 μm; (b) 167.9 μm; (c) 380.2 μm. The data on the glass beads' particle size distribution: (d) 104.5 μm; (e) 167.9 μm; (f) 380.2 μm.

S6. Test on the distribution of residence time in a packed-bed microreactor

In this experiment, the step tracer method was used to test the liquid residence time distribution in the packed-bed microreactor. A methyl orange solution with a concentration of 20 mg/L was used as a tracer, and the liquid at the outlet of the packed-bed microreactor was detected using an ultraviolet-visible spectrometer (Shimadzu, UV-1800). First the standard curve of absorbance of the tracer methyl orange solution with respect to the concentration was plotted, and then the residence time distribution of the liquid in the packed-bed microreactor was investigated by the step tracer method. The standard absorbance curve of methyl orange solution with respect to concentration is shown in Figure S7.

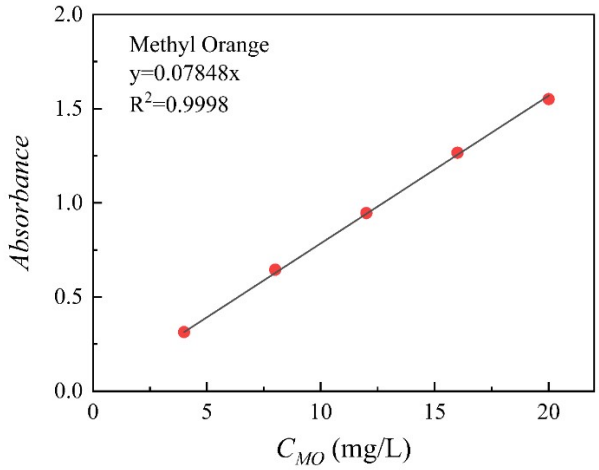

Figure S7 Standard curve of absorbance of methyl orange solution with respect to concentration.

The device for investigating the residence time distribution in the packed-bed microreactor consisted of a water bath, a packed-bed microreactor, a syringe pump, a PFA capillary tube, and a UV-Vis spectrometer. The schematic diagram of the device

is shown in Figure S8. The physical diagram of the packed-bed microreactor is shown in Figure S9.

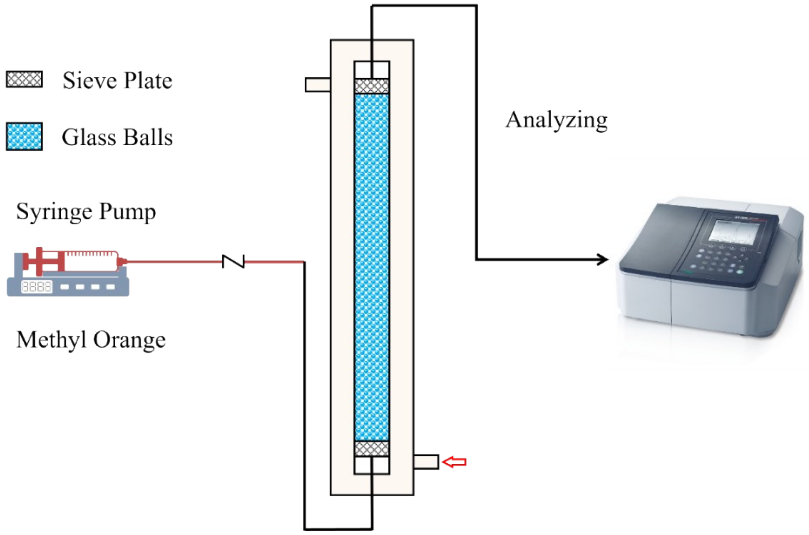

Figure S8 Schematic diagram of the device for investigating the residence time distribution test device for in the glass bead packed packed-bed microreactor.

Figure S9 The physical diagram of the packed-bed microreactor.

The residence time distribution curve of the packed-bed microreactor is shown in Figure S10.

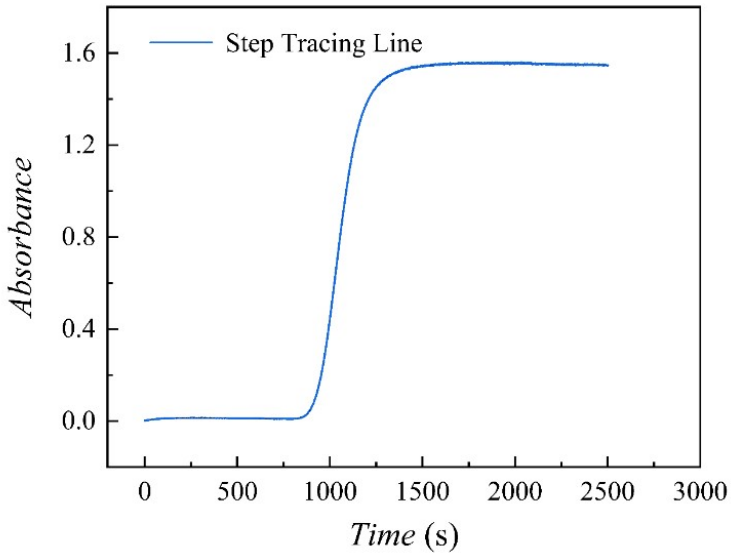

Figure S10 Residence time distribution in the packed-bed microreactor.

In order to better understand the back mixing degree of the tracer in the reactor, the residence time distribution curve of the pulse tracer method in the above figure is denoted as $c(t)$, the highest point of the endpoint is denoted as $c(\infty)$, and the endpoint time is denoted as T. The following equations (Equations (4) - (7)) are used for calculation.

$$E(t) = \frac{dF(t)}{dt} \qquad \text{* MERGEFORMAT (4)}$$

$$F(t) = \frac{c(t)}{c(\infty)} \qquad \text{* MERGEFORMAT (5)}$$

$$\overline{t} = \int_0^\infty tE(t)dt \qquad \text{* MERGEFORMAT (6)}$$

$$\sigma_t^2 = \int_0^\infty t^2 E(t)dt - \overline{t}^2 \qquad \text{* MERGEFORMAT (7)}$$

In Equation (6) and Equation (7), replacing E(t) and F(t) with Equation (4) and Equation (5) respectively give Equations (8) and (9).

$$\bar{t} = \frac{1}{c(\infty)}\int_0^{c(\infty)} t dc(t) = \frac{1}{c(\infty)}[\int_0^T c(\infty)dt - \int_0^T c(t)dt]$$
$$= \int_0^T [1 - \frac{c(t)}{c(\infty)}]dt = \int_0^T [1 - F(t)]dt$$ * MERGEFORMAT (8)

$$\sigma_t^2 = \frac{1}{c(\infty)}\int_0^{c(\infty)} t^2 dc(t) - \bar{t}^2 = \frac{2}{c(\infty)}[\int_0^T tc(\infty)dt - \int_0^T tc(t)dt] - \bar{t}^2$$
$$= 2\int_0^T t[1 - \frac{c(t)}{c(\infty)}]dt - \bar{t}^2 = 2\int_0^T t[1 - F(t)]dt - \bar{t}^2$$ * MERGEFORMAT (9)

By using the above equations to calculate the residence time distribution curve of the packed-bed microreactor in Figure S8, the mathematical expected value ($\bar{t}$) can be obtained as 1068.97 and the variance value (σ_t^2) as 13413.1391. Substituting these two values into the following equations (Equations (10) and (11)), the Bodenstedt number (*Bo*) can be calculated.

$$\sigma^2 = \frac{\sigma_t^2}{\bar{t}^2}$$ * MERGEFORMAT (10)

$$Bo = \frac{2}{\sigma^2}$$ * MERGEFORMAT (11)

Finally *Bo* number was calculated to be 170.38. According to the literature, when *Bo* is more than 100, the axial diffusion of the fluid in the reactor can be ignored, which indicates that the back mixing in the reactor is relatively small and can be approximately regarded as a plug flow.[3] Dibenzyl ether can be oxidized by nitric acid to produce benzaldehyde and further oxidized to form benzoic acid. For the consecutive reaction, the plug flow can effectively regulate the reaction process, which is beneficial to increase the conversion of reactants and improve the selectivity of the main product.

S7. Estimation of the *Ha* number when the mixed liquid phase initially enters the packed-bed microreactor

Table S3 The relevant physical properties of the *Ha* number

	Unit	Value
ρ_a, density of aqueous phase	kg/m^3	1.2600×10^3
ρ_o, density of organic phase	kg/m^3	1.0428×10^3
μ_a, viscosity of aqueous phase	Pa·s	8.9000×10^{-4}(approx.)
μ_o, viscosity of organic phase	Pa·s	8.7190×10^{-3}
D_{12}, diffusivity of HNO_3 in DBE	m^2/s	1.0000×10^{-9}(approx.)

Ha number was estimated when the mixed liquid phase just entered the packed-bed microreactor. The particle size of the particles in the packed-bed microreactor was 104.5 μm, which was taken as the diameter of characteristic channel (d).[4] Assuming the particles are hydrophobic, the effective volume of the bed was obtained by dividing the water volume by the water density, resulting in a porosity (ε) of 35.66% for the packed-bed microreactor. Assuming that the pore channels and particle distribution were uniform, the packed bed microreactor can be regarded as composed of multiple channels. The apparent flow rate (v) of the liquid phase entering the packed bed microreactor was 8.18×10^{-4} m/s. The calculation of Re_0 is 0.035, indicating strict laminar flow. In this case, the following equations (Equations (12) - (19)) are used to calculate superficial mass transfer (k_L).[4,5]

$$Sh = f_\varepsilon(2+\sqrt{Sh_1^2+Sh_2^2}) \qquad \text{* MERGEFORMAT (12)}$$

$$Sh_1 = 0.664\times Re^{\frac{1}{2}}\times Sc^{\frac{1}{3}} \qquad \text{* MERGEFORMAT (13)}$$

$$Sh_2 = \frac{0.037 \times Re^{0.8} \times Sc}{1 + 2.443 \times Re^{-0.1} \times (Sc^{\frac{2}{3}} - 1} \quad \text{* MERGEFORMAT (14)}$$

$$f_\varepsilon = 1 + 1.5 \times (1 - \varepsilon) \quad \text{* MERGEFORMAT (15)}$$

$$Re = \frac{Re_0}{\varepsilon} \quad \text{* MERGEFORMAT (16)}$$

$$Re_0 = \frac{\rho v d}{\mu} \quad \text{* MERGEFORMAT (17)}$$

$$Sc = \frac{\mu}{\rho D_{12}} \quad \text{* MERGEFORMAT (18)}$$

$$Sh = \frac{k_L d}{D_{12}} \quad \text{* MERGEFORMAT (19)}$$

The number of *Ha* can be calculated by the Equation (20).

$$Ha = \frac{\sqrt{\frac{2}{m+1} k C_1^{m-1} C_2^n D_{12}}}{k_L} \quad \text{* MERGEFORMAT (20)}$$

The calculation results are shown in Figure S10. The Ha number is less than 0.3, which can be considered to eliminate the influence of mass transfer.

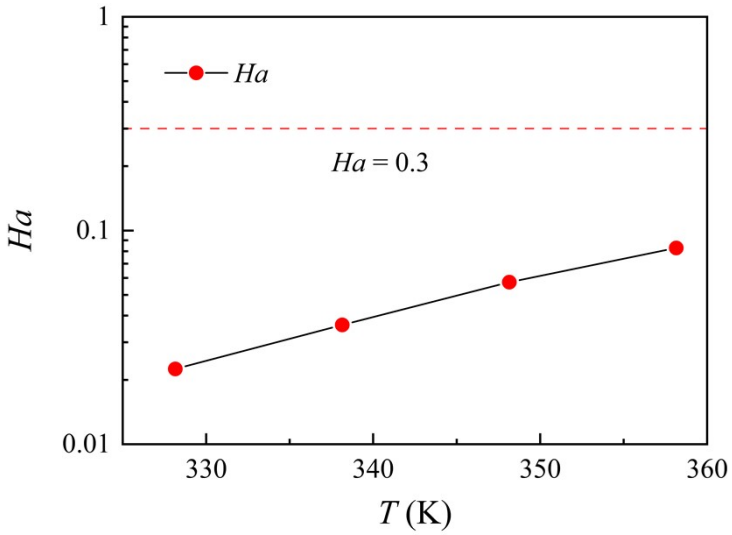

Figure S11 The *Ha* numbers at different temperatures.

References

1 P. Garstecki, M. J. Fuerstman, H. A. Stone and G. M. Whitesides, *Lab Chip*, 2006, **6**, 437-446.

2 T. Thorsen, R. W. Roberts, F. H. Arnold and S. R. Quake, *Phys. Rev. Lett.*, 2001, **86**, 4163-4166.

3 N. M. Kashid, in *Microstructured Devices for Chemical Processing*, eds. A. RENKEN and L. KIWI-MINSKER, Wiley‐VCH Verlag GmbH & Co. KGaA, Weinheim, 2014,vol. 8, pp. 89-128.

4 B. Tidona, S. Desportes, M. Altheimer, K. Ninck and P. R. von Rohr, *Int. J. Heat Mass Transf.*, 2012, **55**, 522-530.

5 V. GNIELINSKI, *Chem. Ing. Tech.*, 1980, **52**, 228-236.